


Lattice Boltzmann finite-difference-based model for fully nonlinear electrohydrodynamic deformation of a liquid droplet

Himadri Sekhar Basu  and Sasidhar Kondaraju ^{*}

School of Mechanical Sciences, Indian Institute of Technology Bhubaneswar, Khordha, Odisha-752050, India

Supreet Singh Bahga 

Department of Mechanical Engineering, Indian Institute of Technology Delhi, Hauz Khas, New Delhi 110016, India



(Received 29 January 2023; accepted 26 May 2023; published 23 June 2023)

Electric field-induced flows involving multiple fluid components with a range of different electrical properties are described by the coupled Taylor-Melcher leaky-dielectric model. We present a lattice Boltzmann (LB)-finite difference (FD) method-based hybrid framework to solve the complete Taylor-Melcher leaky-dielectric model considering the nonlinear surface charge convection effects. Unlike the existing LB-based models, we treat the interfacial discontinuities using direction-specific continuous gradients, which prevents the miscalculation arising due to volumetric gradients without directional derivatives, simultaneously maintaining the electroneutrality of the bulk. While fluid transport is recovered through the LB method using a multiple relaxation time (MRT) scheme, the FD method with a central difference scheme is applied to discretize the charge transport equation at the interface, in addition to the electric field governing equations in the bulk and at the interface. We apply the developed numerical model to study the different regimes of droplet deformation due to an external electric field. Similar to the existing analytical and other numerical models, excluding the surface charge convection (SCC) term from the charge transport equation, the present methodology has shown excellent agreement with the existing literature. In addition, the effect of SCC in each of the regimes is analyzed. With the present numerical model, we observe a strong presence of SCC in the oblate deformation regime, contrary to the weak effect on prolate deformations. We further discuss the reason behind such differences in the magnitude of nonlinearity induced by the SCC in all the regimes of deformation.

DOI: [10.1103/PhysRevE.107.065305](https://doi.org/10.1103/PhysRevE.107.065305)

I. INTRODUCTION

The electrically induced flows of a single fluid or multiple fluids are termed as electrohydrodynamic (EHD) flows. [1]. The EHD flows of a liquid-liquid interface under the influence of external electric fields have provided enormous possibilities in scientific and industrial applications. The applications of EHD flows include, but are not limited to, studying the electrocutation and breakup of rain drops during lightning [2–4], ink-jet printing [5–8], electro-spinning and spraying [9–11], manipulation of droplets and bubbles in microchannels [12–14], biomedical and forensic studies [15], and many more. The nature of charge accumulation at the liquid-liquid interface characterizes the EHD flows involving binary immiscible liquids subjected to an external electric field. Charges may build up at the interface due to the migration of free charges from the fluids or the electrodes, or due to the bound charges from the polarization of the fluids. Moreover, the accumulated charges due to the difference in electrical properties of the fluids lead to a discontinuity in electric fields at the interface. As a consequence, the interface becomes electrically stressed. In a limiting case, when both the fluids are perfectly dielectric or the dispersed phase is highly conducting compared to the suspending media, the interface is free of any

electric shear stresses [16]. Consequently, a highly conducting or insulating droplet under the influence of applied electric forces is solely subjected to normal stresses. At the steady state, the surface tension balances the normal electric stresses. Due to the nonuniform electric stresses along the surface, the droplet deforms along the applied electric field to a prolate spheroid [4,17,18].

A more complex dynamics is involved when both the liquids are weakly conducting or leaky-dielectric (LD). For such liquids subjected to external electric fields, the tangential components of electric shear stresses do not vanish as the charges accumulate at the interface. Depending on the strength of such shear stresses, an LD droplet may deform along or normal to the direction of the applied electric fields into a prolate or an oblate spheroid, respectively [19]. The physics behind such deformations and the effects of different fluidic and electrical properties were explained by Melcher and Taylor [1] in their LD model. The LD model includes the transient effects of surface charges to account for the tangential stresses arising from small yet finite surface charges. Such transient effects of the surface charges arise from the balance between the jump in Ohmic currents normal to the interface due to a mismatch in the electrical conductivities and the convection of charges along the interface due to the interfacial fluid velocity. However, to predict the drop deformation, Taylor's analytical model [20] considers up to the first order of perturbations in drop sphericity corresponding to a small electric capillary

^{*}sasidhar@iitbbs.ac.in

number assuming creeping flow, where the electric capillary number is the ratio of electric stresses to surface tension. The analytical model further neglects the change in surface charge convection with time. Consequently, discrepancies arise between the experiments by Torza *et al.* [21] and Vizika and Saville [19] and the predictions obtained from the linear model. Second-order linear extensions of Taylor's analytical model developed by neglecting the surface charge convection (SCC) by Ajayi [22] also failed to resolve the discrepancies between the linear theory and experiments. A more recent approach by Das and Santilion [23] included the transient charge transport and SCC providing better accuracy to the existing small deformation theories. The second-order analytical predictions further reduced the discrepancy between analytical predictions and experiments. Nonetheless, the linear theories become invalid at larger deformations corresponding to stronger electric fields due to the dominant SCC-induced nonlinearity [18,24]. Hence, seeking numerical solutions for such complex dynamics become inevitable.

In the LD model proposed by Melcher and Taylor [1], SCC is nonlinearly coupled to the tangential component of the electric stresses through the jump in the electric field and current density at the interface. As such, it is a challenging task, both analytically and numerically, to model the effect of SCC corresponding to stronger electric fields when the deformations are large. Despite the challenges, attempts have been made to obtain the numerical predictions of the EHD flows in electrorotation and deformation of droplets and jets [25–31]. The first reported decoupled numerical study using the finite element method (FEM) by Tsukada *et al.* [25] showed good agreement with theory and experiments for small deformations. Feng and Scott [26] solved the complete LD model using FEM considering nonphysical fluid parameters to address the discrepancy between the theory and experiments. However, they also mentioned the importance of incorporating SCC in numerical models. Finite volume (FV) and FD approaches coupled with slightly diffused front-tracking schemes like volume-of-fluid and level-set methods have also been reported to study the EHD deformation of drops and EHD jets [13,28,29]. Sharp interface capturing schemes like the ghost fluid method (GFM) have been shown to mimic the experiments with better accuracy [29,32] due to better treatment of interfacial discontinuities. Das and Santilion [31] solved the coupled LD model, including SCC, to simulate the electrorotation problem using the boundary element method. They further argued that the key to mimicking the experiments on large deformations and electrorotation is the inclusion of SCC. Nonetheless, only a few numerical models have been reported to solve the complete LD model considering the effect of SCC.

In contrast to the conventional computational fluid dynamics-based methods mentioned above, the LB method provides better scalability and computational efficiency. Moreover, explicit front-tracking schemes are unnecessary while dealing with multifluid dynamical systems. Most of the LB-based numerical models reported in the literature solve the decoupled equations for EHD flows without considering the effects of SCC [33–38]. Lauricella *et al.* [34] solved the simplified LD model to study the EHD jet of non-Newtonian fluids. Liu *et al.* [39] proposed to decouple the problem in two

different ways: for weakly conducting cases, Ohm's law was solved, while perfectly dielectric cases involve the solution of Gauss' law. Luo *et al.* [40] solved the coupled problem for multiphase cases throughout the domain in LBM without considering the directional effects. However, they failed to address the dominance of SCC in oblate cases. Moreover, their model failed to maintain the electroneutrality of the bulk. Furthermore, none of the existing LB-based models has been able to explain the effect of SCC in different regimes considering the fully nonlinear symmetry-breaking charge shocks in EHD flows.

In the present work, we propose a hybrid LB-FD-based framework to solve the completely coupled equations of the Taylor-Melcher LD model. The present LB-based model solves the fully coupled governing equations involving multiple liquid components maintaining the electro-neutrality of the bulk and simultaneously prevents the miscalculations arising due to volumetric gradients. The fluid transport has been solved using the LB method with an MRT scheme introduced by d'Humières *et al.* [41]. We implement an improved color-gradient scheme to address the interfacial phenomena devised by Halliday *et al.* [42,43]. The continuous form of the charge transport equation at the interface is solved using the FD method without neglecting the normal and surface directional derivatives. Similarly, Ohm's law in the bulk and continuous form of Gauss' law with normal directional derivative at the interface is solved simultaneously using the FD method to obtain the electric field distribution in the domain. We validate the model by comparing the results from existing theoretical and numerical models where the effect of SCC has not been considered. Next, we simulate cases with SCC and provide an explanation of the differences in nonlinearity induced by the SCC in different deformation regimes.

The present article is organized as follows. In Sec. II, we discuss the governing equations in the LD model for EHD flows. Section III is dedicated to the details of the present numerical methodology. Finally, in Sec. IV, we present the predictions of EHD deformation of droplets from the present model and verify the validity of the results against theoretical and other numerical solutions available in the literature. In this section, we further explain the effect of SCC on deformation in different regimes.

II. MATHEMATICAL FORMULATIONS

The physics of EHD flows are described by the Taylor-Melcher leaky-dielectric model [1,17]. The governing equations for this model involve mass and momentum conservation for fluid transport due to electrodynamic forces, conservation of electrical charges, and an additional equation for the distribution of electric potential in the flow field.

For a binary immiscible fluid system, assuming the system to be isothermal and incompressible for both phases, the governing equations for fluid transport are

$$\nabla \cdot \mathbf{u} = 0, \quad (1)$$

$$\frac{\partial \rho \mathbf{u}}{\partial t} + \nabla \cdot (\rho \mathbf{u} \mathbf{u}) = -\nabla p + \nabla \cdot [\mu(\nabla \mathbf{u} + \nabla \mathbf{u}^T)] + \mathbf{f}_v + \mathbf{f}_e, \quad (2)$$

where ρ , \mathbf{U} , p , and μ denote the density, velocity vector, pressure, and dynamic viscosity of the fluid, respectively. In CFD, to model the interface between such immiscible fluids, surface forces are interpreted as volumetric forces (\mathbf{f}_γ) as [44]

$$\mathbf{f}_\gamma = \gamma \kappa \mathbf{n} \delta_s, \quad (3)$$

where γ and κ represent the coefficient of surface tension and curvature of the interface, respectively. \mathbf{n} is the unit vector pointing in the direction normal to the fluid-fluid interface. δ_s is a Dirac-delta function and ensures that the forces only act on the interface.

Electrical forces (\mathbf{f}_e) are calculated from the Maxwell stress tensor (σ_M). The stress tensor is expressed as

$$\sigma_M = \epsilon (\mathbf{E}\mathbf{E} - \frac{1}{2}(\mathbf{E} \cdot \mathbf{E})\mathbf{I}), \quad (4)$$

where ϵ and \mathbf{I} represent the absolute electrical permittivity of a fluid medium and a second-order unit tensor, respectively. \mathbf{E} is the net electric field due to the superimposition of an externally applied electric field and internal generation of potential due to charge accumulation at the fluid-fluid interface. In Eq. (4), the first term represents stress due to Coulombic forces, while the second term is due to the gradient in polarizability.

Electrostatic forces are obtained by applying the divergence operator on the Maxwell stress tensor as

$$\begin{aligned} \mathbf{f}_e &= \nabla \cdot \sigma_M \\ &= [\nabla \cdot (\epsilon \mathbf{E})]\mathbf{E} - \frac{1}{2}(\mathbf{E} \cdot \mathbf{E})\nabla \epsilon + \frac{1}{2}(\mathbf{E} \cdot \mathbf{E})\nabla \left(\rho \frac{\partial \epsilon}{\partial \rho} \right), \end{aligned} \quad (5)$$

where the first term on the right represents the Coulombic force acting along the electric field. The second and last terms are the dielectric force and electrostrictive force, respectively. The last term is deemed part of the pressure and is usually neglected for an incompressible, isothermal flow.

In EHD flows, the effects of magnetic induction are negligible due to small dynamic currents. Hence, the electric field intensity (\mathbf{E}) in the medium is irrotational and can be expressed as

$$\nabla \times \mathbf{E} = 0. \quad (6)$$

Consequently, in a fluid with dielectric constant ϵ , the Gauss' law can be expressed in terms of electric displacement vector (\mathbf{D}) as

$$\nabla \cdot \mathbf{D} = \nabla \cdot (\epsilon \mathbf{E}) = \rho_e, \quad (7)$$

where ρ_e is the volumetric free charge density. The electric field $\mathbf{E} = -\nabla \phi$ where ϕ is the electric potential. As such, the charge conservation equation in the bulk for an incompressible fluid becomes

$$\frac{D\rho_e}{Dt} + \nabla \cdot \mathbf{J} = \frac{\partial \rho_e}{\partial t} + \mathbf{u} \cdot \nabla \rho_e + \nabla \cdot (\sigma \mathbf{E}) = 0. \quad (8)$$

Here, $\mathbf{J} = \sigma \mathbf{E}$ is the current density due to electrical conduction. $D/Dt = \partial/\partial t + \mathbf{u} \cdot \nabla$ is the material derivative, and σ represents the electrical conductivity of the fluid. For homogeneous electrical properties of the fluid, the bulk of the medium is free of any unbound charge. Under such a condition of the electroneutrality at steady state Eq. (8) reduces to

$$\nabla \cdot (\sigma \mathbf{E}) = 0. \quad (9)$$

The charge transport and the electric field intensity at the interface need separate attention for a complete description of the underlying physics. The continuity of the tangential component of the electric field at the interface leads to

$$\mathbf{n} \times [\mathbf{E}] = 0, \quad (10)$$

where $[\cdot]$ denotes the jump of properties across the interface from one fluid medium to another. In contrast, the jump of the normal component of the electric displacement vector at the interface due to discontinuity is expressed as

$$\mathbf{n} \cdot [\mathbf{D}] = \mathbf{n} \cdot [\epsilon \mathbf{E}] = q_s, \quad (11)$$

where q_s is the free charge at the interface per unit surface area. The conservation of free charges at the interface leads to [1,23]

$$\frac{\partial q_s}{\partial t} + \nabla_s \cdot (\mathbf{u}q_s) = -\nabla_s \cdot \mathbf{J}, \quad (12)$$

where

$$\nabla_s = \nabla - \nabla_n \quad (13)$$

is the surface-divergence operator. ∇_n denotes the gradient in the direction normal to the interface and is expanded as

$$\nabla_n = \mathbf{n}(\mathbf{n} \cdot \nabla). \quad (14)$$

Equation (12) can be further simplified using the relations (13) and (14) to [17]

$$\frac{\partial q_s}{\partial t} + \nabla_s \cdot (\mathbf{u}q_s) = -[\sigma \cdot \mathbf{E}]\mathbf{n}, \quad (15)$$

As can be observed, Eqs. (11) and (15) are jump equations at the interfacial boundary. Solving such equations can be complicated due to diffused interface constructed by the numerical methods. Hence, the jump terms are replaced with continuous volumetric gradients normal to the interface ($[\cdot] \cdot \mathbf{n} \equiv \nabla_n \cdot (\cdot)$) [43,44]. The volumetric forms of the equations using the expansion (14) are

$$\nabla_n \cdot (\epsilon \mathbf{E}) = \mathbf{n}(\mathbf{n} \cdot \nabla) \cdot (\epsilon \mathbf{E}) = \rho_e, \quad (16)$$

$$\frac{\partial \rho_e}{\partial t} + \nabla_s \cdot (\mathbf{u}\rho_e) = -\mathbf{n}(\mathbf{n} \cdot \nabla) \cdot (\sigma \mathbf{E}). \quad (17)$$

Scaling analysis and nondimensional form of governing equations

Multiphysics interactions corresponding to individual physical processes in EHD flows occur at different scales in space and time. Hence a scaling analysis of the governing equations can provide a better understanding of the underlying processes. Such an analysis, moreover, helps to find an improved choice of time steps for the numerical simulations. In the present context, there are four important timescales: the viscous timescale t_v , the capillary timescale t_c , the charge relaxation timescale t_r , and the electroviscous flow timescale t_{ev} . These timescales for the k th component are defined as

$$t_{v,k} = \frac{l^2}{\nu_k}, \quad t_{c,k} = \frac{l\mu_k}{\gamma}, \quad t_{r,k} = \frac{\epsilon_k}{\sigma_k}, \quad t_{ev,k} = \frac{\mu_k}{\epsilon_k E_a^2}, \quad (18)$$

where l , ν , and E_a are the characteristic lengthscale, the kinematic viscosity of the corresponding fluid, and the magnitude

of the applied external electric field, respectively. The subscripts $k = i$ and $k = o$ denote the dispersed and continuous phases, respectively. The important velocity scales are the viscous velocity ($u_{v,k}$), capillary flow velocity ($u_{c,k}$), velocity of charge relaxation ($u_{r,k}$), and the electroviscous velocity ($u_{ev,k}$). These velocity scales are defined as

$$u_{v,k} = \frac{v_k}{l}, \quad u_{c,k} = \frac{\gamma}{\mu_k}, \quad u_{r,k} = \frac{l\sigma_k}{\epsilon_k}, \quad u_{ev,k} = \frac{\epsilon_k E_a^2 l}{\mu_k}. \quad (19)$$

In EHD flows, the electroviscous velocity ($u_{ev,o}$) of the continuous phase is one of the most dominant velocity scales [1]. Hence, we use $t_{ev,o}$, E_a , and $u_{ev,o}$ as the characteristic timescale, electric field intensity, and velocity scale, respectively, to derive the dimensionless form of the governing equations. Other scaling factors are defined with respect to the properties of the continuous phase as

$$\begin{aligned} \nabla &= \frac{1}{l} \nabla^*, & \nabla_s &= \frac{1}{l} \nabla_s^*, & \rho &= \rho_o \rho^*, & p &= \epsilon_o E_a^2 p^*, \\ \epsilon &= \epsilon_o \epsilon^*, & \sigma &= \sigma_o \sigma^*, & \rho_e &= \frac{\epsilon_o E_a}{l} \rho_e^*, & q_s &= \epsilon_o E_a q_s^*. \end{aligned} \quad (20)$$

Here the superscript $*$ denotes the dimensionless parameters. Using these transformations, the dimensionless governing equations in the bulk become

$$\nabla^* \cdot \mathbf{u}^* = 0, \quad (21)$$

$$\begin{aligned} \text{Re}_{ev,o} \text{Ca}_{e,o} \left[\frac{\partial \rho^* \mathbf{u}^*}{\partial t^*} + \nabla^* \cdot (\rho^* \mathbf{u}^* \mathbf{u}^*) \right] \\ = \text{Ca}_{e,o} [-\nabla^* p^* + \nabla^* \cdot [\mu^* (\nabla^* \mathbf{u}^* + \nabla^* \mathbf{u}^{*T})]] + \mathbf{f}_e^* \\ + \kappa^* \mathbf{n} \delta_s^*, \end{aligned} \quad (22)$$

$$\nabla^* \cdot (\sigma^* \mathbf{E}^*) = 0. \quad (23)$$

Here we compare the strength of individual physical processes with respect to the interfacial phenomena for the momentum transport equations. $\text{Ca}_{e,o}$ and $\text{Re}_{ev,o}$ represent the electric capillary number and electroviscous Reynolds number of the outer or continuous phase, respectively. While the electric capillary number (Ca_e) is defined as the ratio of the timescale of the capillary action and electroviscous effects, electroviscous Reynolds number (Re_{ev}) is the ratio of the viscous and the electroviscous timescales. These nondimensional numbers for the continuous phase are expressed as

$$\text{Ca}_{e,o} = \frac{t_{c,o}}{t_{ev,o}} = \frac{\epsilon_o E_a^2 l}{\gamma}, \quad (24)$$

$$\text{Re}_{ev,o} = \frac{t_{v,o}}{t_{ev,o}} = \frac{\rho_o \epsilon_o E_a^2 l^2}{\mu_o^2}. \quad (25)$$

Similarly, the dimensionless form of the equations at the interface becomes

$$\frac{\epsilon_o}{\sigma_o \tau_p} \frac{\partial q_s^*}{\partial t^*} + \text{Re}_{e,o} \nabla_s^* \cdot (\mathbf{u}^* q_s^*) = -[\sigma^* \mathbf{E}^*] \cdot \mathbf{n}, \quad (26)$$

$$\mathbf{n} \cdot [\epsilon^* \mathbf{E}^*] = q_s^*, \quad (27)$$

wherein the strength of all the terms is compared with respect to the conduction of charges in the charge transport equation.

Here, the electric Reynolds number ($\text{Re}_{e,k}$) dictates the competition at the interface between the effect of surface charge convection (SCC) and the conduction of charges from the bulk. The electric Reynolds number ($\text{Re}_{e,o}$) for the continuous phase is defined as the ratio of the charge relaxation time scale and the electroviscous timescale as

$$\text{Re}_{e,o} = \frac{t_{r,o}}{t_{ev,o}} = \frac{\epsilon_o^2 E_a^2}{\mu_o \sigma_o}. \quad (28)$$

In addition, the ratios of physical and electrochemical properties of the dispersed and continuous phases, like dynamic viscosity (λ_μ), electrical permittivity (λ_p), and electrical conductivity (λ_c), play a key role in EHD flows and are defined as

$$\lambda_\mu = \frac{\mu_i}{\mu_o}, \quad \lambda_p = \frac{\epsilon_i}{\epsilon_o}, \quad \lambda_c = \frac{\sigma_i}{\sigma_o}. \quad (29)$$

III. NUMERICAL METHOD

The present study involves the numerical modeling of EHD flows of multiple immiscible liquid components. A hybrid method is adopted to solve the coupled equations. This method involves solving each transport phenomenon using a different numerical method [43,45]. Fluid transport equations [Eqs. (1) and (2)] are recovered by solving the discrete Boltzmann equation using MRT-LBM with a color-gradient scheme to capture the interfacial dynamics. The surface convection of charges [Eq. (17)] and electric field governing equation in the bulk [Eq. (9)] and at the interface [Eq. (16)] are solved using the finite difference method. These methods are explained in detail in the following sections.

A. Hydrodynamics using LBM

The present simulations involve the EHD flow of multiple fluid components. Hence an existing hybrid LB-based numerical model [45] is modified accordingly by implementing multicomponent LBM [46] based on the color-gradient model initially proposed by Gunstensen *et al.* [47]. A D2Q9 velocity discretisation scheme (Fig. 1) is adopted for the two-dimensional (2D) simulations. An MRT scheme finally solves the discrete evolution equations [46,48,49]. The solution of the fluid evolution equation involves three steps, namely, collision, recoloring and segregation, and streaming.

In MRT-LBM for incompressible, laminar flow with an external force, the collision equation is

$$f_i^\dagger(\mathbf{x}, t) = f_i(\mathbf{x}, t) - \mathbf{M}^{-1} \mathbf{S} [\mathbf{m}(\mathbf{x}, t) - \mathbf{m}^{\text{eq}}(\mathbf{x}, t)] \Delta t_f + F_i \Delta t_f, \quad (30)$$

where f_i and f_i^\dagger are the pre and postcollision packet density distribution function in the direction of i , respectively. \mathbf{x} , \mathbf{c}_i , and Δt_f denote the position vector, the discrete lattice velocity in the direction of i , and the lattice time-step for fluid evolution, respectively. The second term on the right represents the MRT collision operator [41,48,50]. Compared to the Bhatnagar-Gross-Krook (BGK) collision operator in single relaxation time (SRT) schemes, an MRT collision

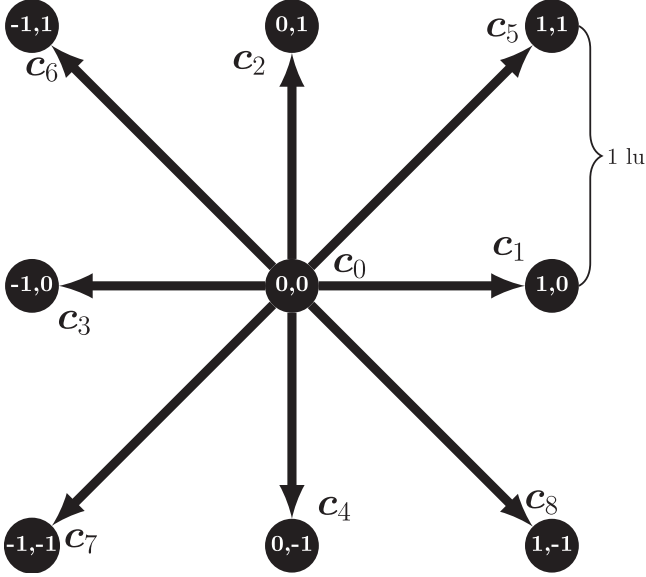


FIG. 1. D2Q9 lattice velocity scheme

operator enhances the stability of the model by reducing non-physical spurious currents at the interface [51]. The external forces in the lattice direction i are added through the forcing term F_i .

For the D2Q9 lattice, the discrete velocities are

$$\mathbf{c}_i = \begin{cases} (0, 0) & \text{for } i = 0, \\ (\pm 1, 0)c, (0, \pm 1)c & \text{for } i = 1-4, \\ (\pm 1, \pm 1)c & \text{for } i = 5-8, \end{cases} \quad (31)$$

where c represents the lattice speed and is defined as $c = \Delta x / \Delta t_f$ with Δx being the lattice distance in lattice units. In the present simulations, Δx and Δt_f are assumed unity for simplicity, thus leading to $c = 1$.

The moments \mathbf{m} and \mathbf{m}^{eq} are the linear mappings of f and the equilibrium distribution function (f^{eq}) on moment space, respectively, and is expressed as

$$\mathbf{m} = \mathbf{M}f, \quad (32)$$

$$\mathbf{m}^{\text{eq}} = \mathbf{M}f^{\text{eq}}, \quad (33)$$

where \mathbf{M} is a 9×9 Gram-Schmidt transformation matrix [46] such that $\mathbf{M}^{-1}\mathbf{M} = \mathbf{I}$ assuming \mathbf{M}^{-1} exists. The relaxation parameters for different moments are included in \mathbf{S} , where \mathbf{S} is a nonnegative diagonal matrix. Following Kruger *et al.* [46], we use \mathbf{S} as

$$\mathbf{S} = \text{diag}\left(0, 1.63, 1.14, 0, 1.92, 0, 1.92, \frac{1}{\tau_{\text{LB}}}, \frac{1}{\tau_{\text{LB}}}\right). \quad (34)$$

The relaxation time for the fluid equation (τ_{LB}) is calculated from

$$\tau_{\text{LB}} = \frac{\nu}{c_s^2 \Delta t_f} + 0.5, \quad (35)$$

where ν is the kinematic viscosity of the fluid in lattice units. c_s represents the speed of sound in lattice units and is related to lattice velocity c as $c = \sqrt{3}c_s$.

The equilibrium distribution function f_i^{eq} for fluid flow [52] is defined as

$$f_i^{\text{eq}}(\mathbf{x}) = \omega_i \rho(\mathbf{x}) \left[1 + 3 \frac{\mathbf{c}_i \cdot \mathbf{u}}{c^2} + \frac{9}{2} \frac{(\mathbf{c}_i \cdot \mathbf{u})^2}{c^4} - \frac{3}{2} \frac{u^2}{c^2} \right], \quad (36)$$

where ρ and \mathbf{u} are the macroscopic density and velocity, respectively, in lattice units. For the D2Q9 scheme, the weight coefficients ω_i are written as

$$\omega_i = \begin{cases} 4/9 & \text{for } i = 0, \\ 1/9 & \text{for } i = 1-4, \\ 1/36 & \text{for } i = 5-8. \end{cases} \quad (37)$$

The forcing term (F_i) is appended to the LB evolution equation [Eq. (30)] using an exact difference scheme [53] as

$$F_i = f_i^{\text{eq}}(\rho, \mathbf{u} + \mathbf{F} \Delta t_f / \rho) - f_i^{\text{eq}}(\rho, \mathbf{u}), \quad (38)$$

where \mathbf{F} is the total external volumetric force in lattice units.

Color-gradient model for the construction of the interface

To construct the interface between two immiscible fluids, the interfacial body force (\mathbf{F}_γ) is calculated using the continuum surface force (CSF) model proposed by Brackbill *et al.* [54] as

$$\mathbf{F}_\gamma = -\frac{1}{2} \alpha \kappa \nabla \rho_N. \quad (39)$$

Here, α is the surface tension parameter. ρ_N is the normalized density used to segregate or colorize individual fluids. For a binary fluid system, ρ_N is defined by the local densities of individual components as

$$\rho_N(\mathbf{x}, t) = \frac{\rho_r(\mathbf{x}, t) - \rho_b(\mathbf{x}, t)}{\rho_r(\mathbf{x}, t) + \rho_b(\mathbf{x}, t)}, \quad (40)$$

where the subscripts r and b indicate red and blue fluid components, respectively. As such, $-1 < \rho_N < 1$.

Subsequently, the recoloring scheme by Latva-Kokko and Rothman [55] is applied for phase segregation and the construction of the interface. In contrast to the original Gunstensen model [47], the algorithm provided by Latva-Kokko and Rothman produces less spurious current at the interface and is free of the lattice pinning problem [43,56]. The postsegregation distribution functions of red and blue fluids become

$$f_{i,r}^{\dagger\dagger}(\mathbf{x}, t) = \frac{\rho_r}{\rho} f_{i,r}^{\dagger}(\mathbf{x}, t) + \beta_{\text{LKR}} \frac{\rho_r \rho_b}{\rho} \omega_i \frac{\mathbf{c}_i \cdot \nabla \rho_N}{|\nabla \rho_N|}, \quad (41)$$

$$f_{i,b}^{\dagger\dagger}(\mathbf{x}, t) = \frac{\rho_b}{\rho} f_{i,r}^{\dagger}(\mathbf{x}, t) - \beta_{\text{LKR}} \frac{\rho_r \rho_b}{\rho} \omega_i \frac{\mathbf{c}_i \cdot \nabla \rho_N}{|\nabla \rho_N|}. \quad (42)$$

Here, β_{LKR} is the segregation parameter to control the thickness of the interface. The existing literature [43,56] suggests the value of β_{LKR} equal to 0.7 to confine a sharp interface of thickness $\sim 4-5$ lattice units. Moreover, such a value of β_{LKR} helps to minimize the spurious currents at the interface and reproduces correct interfacial behavior. Hence, in the present work, we use $\beta_{\text{LKR}} = 0.7$.

Postsegregation, the streaming step for fluid component k , is obtained as

$$f_{i,k}(\mathbf{x} + \mathbf{c}_i \Delta t_f, t + \Delta t_f) = f_{i,k}^{\dagger\dagger}(\mathbf{x}, t). \quad (43)$$

The total packet density distribution function f_i is calculated from the distribution function of the individual components as

$$f_i = \sum_k f_{i,k}. \quad (44)$$

The macroscopic variables like the total density (ρ), the density of the k th-component (ρ_k), velocity (\mathbf{u}), and pressure (p) are calculated as

$$\rho = \sum_i f_i, \quad \rho_k = \sum_i f_{i,k}, \quad \mathbf{u} = \frac{1}{\rho} \sum_i f_i \mathbf{c}_i, \quad p = \rho c_s^2. \quad (45)$$

B. Charge transport Using FDM

Considering electroneutrality in the bulk, the solution of Eq. (17) is sufficient to obtain the charge distribution in the domain. A second-order central difference scheme is used to spatially discretize the continuum equation, while a first-order forward difference scheme is used for temporal discretization. Finally, after rearranging, the discretized equation for charge transport becomes

$$\begin{aligned} & \frac{\rho_e^{(k+1)}(i, j) - \rho_e^{(k)}(i, j)}{\Delta t} + u_x(i, j) \frac{\hat{\delta}_x \rho_e(i, j)}{2(\Delta x)} + u_y(i, j) \frac{\hat{\delta}_y \rho_e(i, j)}{2(\Delta y)} + \rho_e(i, j) \left(\frac{\hat{\delta}_x u_x(i, j)}{2(\Delta x)} + \frac{\hat{\delta}_y u_y(i, j)}{2(\Delta y)} \right) \\ & - \rho_e(i, j) \left(n_x^2(i, j) \frac{\hat{\delta}_x u_x(i, j)}{2(\Delta x)} + n_x(i, j) n_y(i, j) \frac{\hat{\delta}_y u_x(i, j)}{2(\Delta y)} + n_x(i, j) n_y(i, j) \frac{\hat{\delta}_x u_y(i, j)}{2(\Delta x)} + n_y^2(i, j) \frac{\hat{\delta}_y u_y(i, j)}{2(\Delta y)} \right) \\ & - u_x(i, j) \left(n_x^2(i, j) \frac{\hat{\delta}_x \rho_e(i, j)}{2(\Delta x)} + n_x(i, j) n_y(i, j) \frac{\hat{\delta}_y \rho_e(i, j)}{2(\Delta y)} \right) - u_y(i, j) \left(n_x(i, j) n_y(i, j) \frac{\hat{\delta}_x \rho_e(i, j)}{2(\Delta x)} + n_y^2(i, j) \frac{\hat{\delta}_y \rho_e(i, j)}{2(\Delta y)} \right) \\ & = \sigma(i, j) \left(n_x^2(i, j) \frac{\hat{\delta}_x E_x(i, j)}{2(\Delta x)} + n_x(i, j) n_y(i, j) \frac{\hat{\delta}_y E_x(i, j)}{2(\Delta y)} + n_x(i, j) n_y(i, j) \frac{\hat{\delta}_x E_y(i, j)}{2(\Delta x)} + n_y^2(i, j) \frac{\hat{\delta}_y E_y(i, j)}{2(\Delta y)} \right) \\ & + E_x(i, j) \left(n_x^2(i, j) \frac{\hat{\delta}_x \sigma(i, j)}{2(\Delta x)} + n_x(i, j) n_y(i, j) \frac{\hat{\delta}_y \sigma(i, j)}{2(\Delta y)} \right) + E_y(i, j) \left(n_x(i, j) n_y(i, j) \frac{\hat{\delta}_x \sigma(i, j)}{2(\Delta x)} + n_y^2(i, j) \frac{\hat{\delta}_y \sigma(i, j)}{2(\Delta y)} \right), \end{aligned} \quad (46)$$

where $\hat{\delta}$ is the central-difference operator [57] defined as

$$\hat{\delta}_x \sigma(i, j) = \sigma(i + 1, j) - \sigma(i - 1, j).$$

The discretized equation [Eq. (46)] is solved using an alternating direction explicit (ADE) method [57] for the solution of ρ_e . The ADE method is chosen due to the simplicity of implementation and unconditional stability [57].

C. Electric field in the domain using FDM

The electric field in the domain is obtained by solving Ohm's law [Eq. (9)] in the bulk and the volumetric form of Gauss' law at the interface [Eq. (16)] simultaneously. Expanding Eq. (9),

$$\sigma \nabla^2 \phi + \nabla \sigma \cdot \nabla \phi = 0. \quad (47)$$

Discretizing Eq. (47) with a second-order central difference scheme and rearranging, we get the solution for electric potential (ϕ) at node (i, j) as

$$\begin{aligned} \phi(i, j) &= \frac{1}{2(1 + \beta^2)} [\phi(i + 1, j) + \phi(i - 1, j) + \beta^2 [\phi(i, j + 1) + \phi(i, j - 1)]] \\ &+ \frac{1}{8\sigma(i, j)(1 + \beta^2)} [\hat{\delta}_x \sigma(i, j) \hat{\delta}_x \phi(i, j) + \hat{\delta}_y \sigma(i, j) \hat{\delta}_y \phi(i, j)], \end{aligned} \quad (48)$$

where $\beta = \Delta x / \Delta y$ is the grid aspect-ratio. Since the interface is diffused and spread over several grids, we consider the volumetric form of Eq. (11), i.e., Eq. (16), for the solution of the electric field at the interface. Thus, we can capture the discontinuities at the interface retaining the directional behavior. Expanding Eq. (16) and using the relation $\mathbf{E} = -\nabla \phi$, we obtain

$$\epsilon \mathbf{n} \cdot (\mathbf{n} \cdot \nabla) \nabla \phi + \nabla \phi \cdot \mathbf{n} (\mathbf{n} \cdot \nabla) \epsilon = -\rho_e. \quad (49)$$

Similar to Eq. (47), a second-order central difference scheme is used to discretize Eq. (49). Finally, after rearranging the terms, we obtain the solution of ϕ at node (i, j) at the interface at the $k + 1$ th iteration step as

$$\begin{aligned} \phi(i, j)^{k+1} = & \frac{1}{\left[2\epsilon(i, j)\left(\frac{n_x^2(i, j)}{\Delta x^2} + \frac{n_y^2(i, j)}{\Delta y^2}\right)\right]} \left[\rho_e(i, j) + \frac{n_x^2(i, j)}{\Delta x^2} (\epsilon(i, j)[\phi(i+1, j) + \phi(i-1, j)]) \right. \\ & + \frac{1}{4}[\phi(i+1, j) + \phi(i-1, j)] + \frac{n_x(i, j)n_y(i, j)}{4\Delta x\Delta y} [\epsilon(i, j)\delta_{xy}^2\phi(i, j) + \hat{\delta}_x\phi(i, j)\hat{\delta}_y\epsilon(i, j) + \hat{\delta}_y\phi(i, j)\hat{\delta}_x\epsilon(i, j)] \\ & \left. + \frac{n_y^2(i, j)}{\Delta y^2} (\epsilon(i, j)[\phi(i, j+1) + \phi(i, j-1)] + \frac{1}{4}[\phi(i, j+1) + \phi(i, j-1)]) \right]. \end{aligned} \quad (50)$$

The simultaneous iterative solution of these two discretized equations [Eqs. (48) and (50)] in the bulk and at the interface were obtained using the Gauss-Seidel iteration method [57] with a successive overrelaxation (SOR) scheme.

D. Boundary conditions

For all the problems considered in the present study, the interface is sufficiently away from the boundary. As such, the velocities near the domain boundary are negligible. Thus, the hydrodynamics of the problem can be considered periodic in all directions [40]. The periodic boundary condition is implemented through the streaming step for the hydrodynamic problem solved in LBM. Hence, no separate step is required to implement the periodic boundary condition.

The charge transport equation is solved only at the interface surrounded by the bulk and the droplet is stationary at the center of the domain. Moreover, due to the electroneutrality condition, the bulk is assumed to be void of electrical charges. As such, implementing periodic boundary conditions is unnecessary for the charge transport equation.

For the solution of the electric field, Ohm's law [Eq. (9)] is accompanied by a periodic boundary condition in the direction perpendicular to the applied electric field. Such is obtained at a point $(i = 0, j)$ on the left boundary by considering

$$\phi(0, j) = \phi(NX, j), \quad (51)$$

$$\left. \frac{\partial \phi}{\partial x} \right|_{(0, j)} = \left. \frac{\partial \phi}{\partial x} \right|_{(NX, j)}. \quad (52)$$

In discretized form considering the accuracy of $O(\delta x)$, we obtain

$$\phi(0, j) = \phi(NX, j) = \frac{\phi(1, j) + \phi(NX - 1, j)}{2\delta x}. \quad (53)$$

Here, we assume the extreme points of the domain lie at $i = 0$ and $i = NX$ in the direction perpendicular to the applied electric field.

E. Algorithm

The algorithm of the present hybrid LB-FD model is shown in Fig. 2. First, we initialize the computational domain with the fluid and electric properties of each fluid. Typically, the charge transport equations in the bulk and at the interface [Eqs. (8) and (12)] involve smaller timescales compared to fluid transport. Such a difference in timescales does not allow direct coupling of the hydrodynamics with the charge transport. Hence, multiple time iterations for charge transport are required for each time step of fluid transport equations. In contrast, the Gauss' law at the interface [Eq. (11)] and the

Ohmic conduction equation at the bulk [Eq. (9)] are steady-state equations and hence solved simultaneously at each time step of the charge transport equation. For a detailed discussion of a similar algorithm, we refer to our previous publication [45] on electrokinetic instabilities in single-phase flows with conductivity gradients.

IV. RESULTS AND DISCUSSION

In this section, we demonstrate the validity of the present methodology through the simulation of droplet deformation subjected to an external electric field. To validate the model, first we perform a grid independence test using different grid sizes and varying the electric capillary number. Then we study the deformation of a liquid droplet neglecting and considering the SCC term, respectively. Figure 3 shows the schematic of a liquid droplet suspended in another liquid medium in a square periodic domain. The droplet is placed at the center of the domain between two electrodes, which are placed at the top

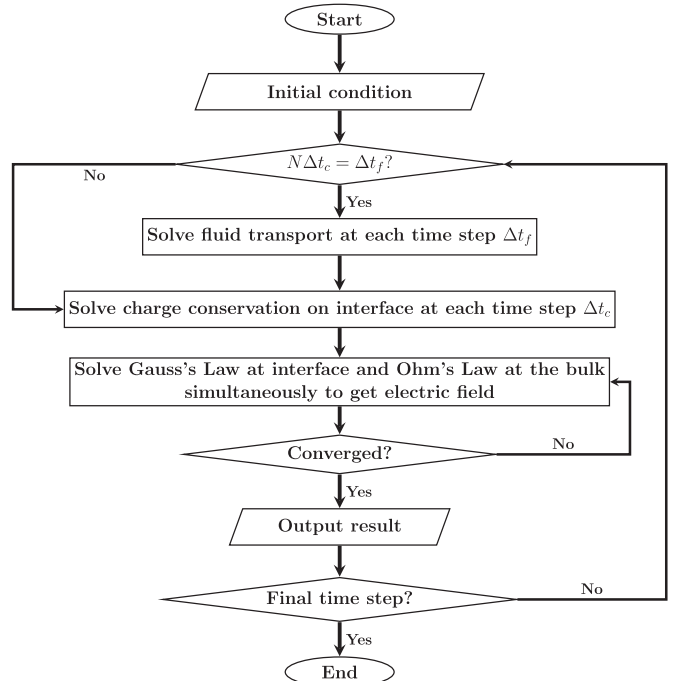


FIG. 2. Algorithm of the present methodology.

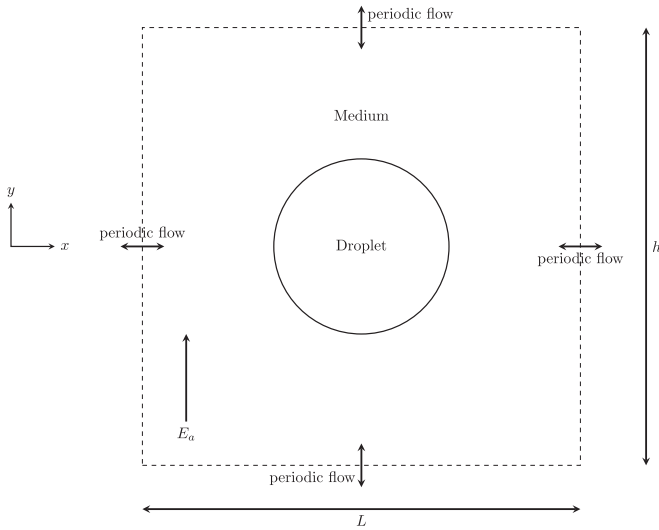


FIG. 3. Schematic of the deformation of a liquid droplet under the influence of electrical forces. The droplet is placed at the center of the domain, surrounded by another continuous liquid component. An external electric field is applied from the bottom towards the top of the domain.

and the bottom. The external electric field is applied from the bottom towards the top of the domain. The sides of the domain ($L = h$) have length $800\mu\text{m}$ and initial diameter (D_d) of the droplet is $160\mu\text{m}$.

For the present study, we vary each fluid’s electrical conductivity (σ) and dielectric constant (ϵ) and their corresponding ratios to demonstrate the effect of different parameters at different conductivity regimes. In addition, the external electric field is varied to study the effects of Ca_e . Other physical properties of the fluids are kept constant unless otherwise mentioned explicitly and are provided in Table I.

A. Grid-independence test

First, we calculated the convergence order from the deformation (D) at three consecutive time steps using [58]

$$\lim_{k \rightarrow \infty} \frac{|D_{k+2} - D_{k+1}|}{|D_{k+1} - D_k|}. \tag{54}$$

TABLE I. Notation and values of the fluids’ physical properties involved in the droplet deformation study due to EHD forces.

Symbol	Description	Value
a	Radius of initially spherical droplet	$7.38 \times 10^{-5} \text{ m}$
γ	Surface tension between the liquid components	$1.31 \times 10^{-3} \text{ N m}^{-1}$
ρ_i	Density of dispersed phase	1000 kg m^{-3}
ρ_o	Density of continuous phase	1000 kg m^{-3}
μ_i	Dynamic viscosity of dispersed phase	$1.4 \times 10^{-3} \text{ Pa s}$
μ_o	Dynamic viscosity of continuous phase	$1.0 \times 10^{-3} \text{ Pa s}$
ϵ_i	Absolute electrical permittivity of dispersed phase	$1.64 \times 10^{-10} \text{ C/V m}$
ϵ_o	Absolute electrical permittivity of continuous phase	$4.69 \times 10^{-11} \text{ C/V m}$
σ_i	Electrical conductivity of dispersed phase for prolate deformation	$4.75 \times 10^{-7} \text{ S/m}$
σ_i	Electrical conductivity of dispersed phase for oblate deformation	$1.75 \times 10^{-7} \text{ S/m}$
σ_o	Electrical conductivity of continuous phase	$1 \times 10^{-7} \text{ S/m}$

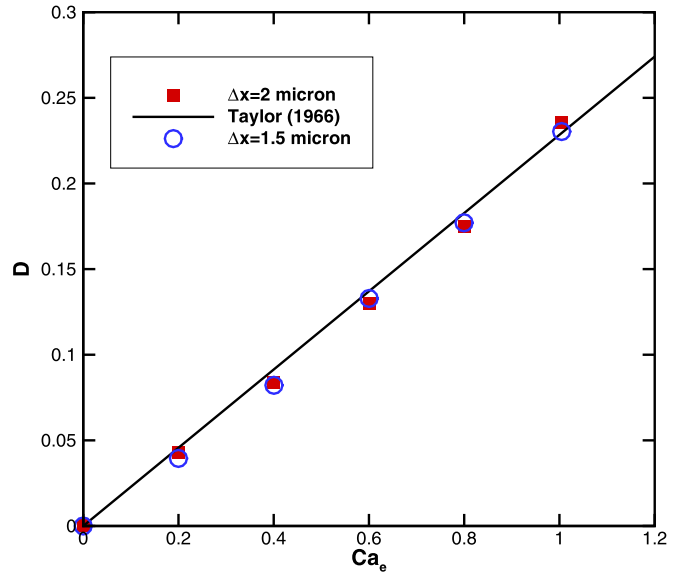


FIG. 4. Deformation as a function of Ca_e using different grid sizes. The solid black line represents Taylor’s analytical results. The red-filled squares and open blue circles represent the cases using grid sizes $2\mu\text{m}$ and $1.5\mu\text{m}$, respectively.

The above expression is evaluated for $Ca_e = 0.4$ using grid sizes $1.5\mu\text{m}$ and $2\mu\text{m}$. In both cases, the value of the expression is 1, suggesting that the present hybrid model converges logarithmically. To validate the choice of grid size, we performed a grid independence test using grid sizes $1.5\mu\text{m}$ and $2\mu\text{m}$. We compare the deformation obtained using different grid sizes with varying capillary numbers in Fig. 4. We observe that, in both cases, the deformation coincides with each other and Taylor’s analytical results. Hence, we simulate the rest of the cases using $2\mu\text{m}$ grid size.

B. Deformation of an LD droplet

To investigate the model’s performance proposed in the present work, we first study the deformation of a leaky-dielectric liquid droplet suspended in another leaky-dielectric liquid medium. As such, the electrical conductivities of both the liquids are of the order 10^{-7} S/m , while the electrical permittivities of the liquids are of the order $10^{-11} - 10^{-10} \text{ C/Vm}$.

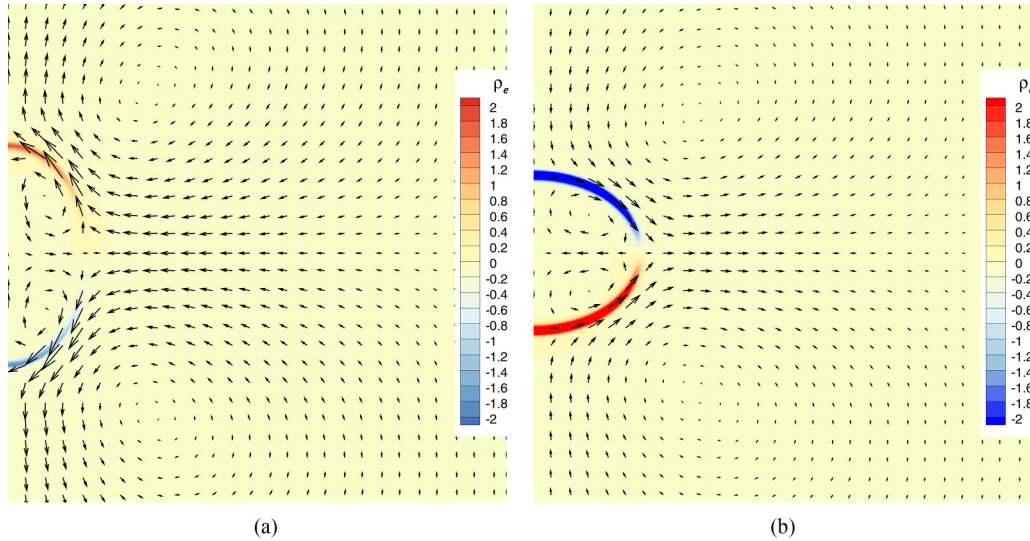


FIG. 5. Contours of deformation, charge distribution, and velocity vectors within and outside of a deformed droplet at $\lambda_p = 3.5$, $\lambda_\mu = 1.40$, and $\text{Ca}_e = 0.8$. (a) Prolate deformation with $\lambda_c = 4.75$ and (b) oblate deformation with $\lambda_c = 1.75$. Positive, zero, and negative charges are indicated with red, yellow, and blue, respectively.

Consequently, the charge relaxation times of both fluids are short compared to the viscous timescale.

In this regime of electrical conductivity, namely, the leaky-dielectric regime, a droplet subjected to a uniform electric field can obtain the shape of an ellipsoid either in the direction of the applied electric field or in the perpendicular direction. Taylor [20] proposed an analytical expression to find EHD deformation of the droplet at steady state from linear stability analysis as

$$D = \frac{L - B}{L + B} = \frac{9\text{Ca}_e f_T(\lambda_c, \lambda_p, \lambda_\mu)}{16(2 + \lambda_c)^2}. \quad (55)$$

Here, D represents the EHD deformation factor of the droplet at the steady state. L and B are the final end-to-end lengths of the droplet at the steady state in the direction parallel and perpendicular to the applied electric field, respectively. The Taylor discriminating function (f_T) to predict the final shape of the droplet is expressed as

$$f_T(\lambda_c, \lambda_p, \lambda_\mu) = \lambda_c^2 + 1 - 2\lambda_p + \frac{3(2 + 3\lambda_\mu)}{5(1 + \lambda_\mu)}(\lambda_c - \lambda_p). \quad (56)$$

Another analytical model by Feng [59] predicted the droplet deformation using asymptotic analysis of first-order approximation. In Feng's model, the analytical expression for droplet deformation is given by

$$D = \frac{\text{Ca}_e f_F(\lambda_c, \lambda_p)}{3(1 + \lambda_c)^2}, \quad (57)$$

where $f_F = \lambda_c^2 + \lambda_c + 1 - 3\lambda_p$ is the discriminating function proposed by Feng [59].

The qualitative nature of the droplet deformations can be inferred from the sign of the discriminating functions. For $f_T > 0$ or $f_F > 0$, the deformation factor (D) is positive and the droplet deforms in the direction of the applied electric field, leading to a prolate shape. In contrast, when $f_T < 0$ or $f_F < 0$, the deformation factor (D) is negative and the droplet

deforms into an oblate shape elongating in the direction perpendicular to the applied electric field.

We compare the physics mentioned above to validate the present methodology with the results obtained from the present simulations. Figure 5(a) shows deformation of a LD droplet with $\lambda_c = 4.75$, $\lambda_p = 3.5$, $\lambda_\mu = 1.4$, and $\text{Ca}_e = 0.8$. With these nondimensional parameters, both f_T and f_F are positive with the values 18.5 and 17.8125, respectively. For such values of the discriminating functions, we observe a prolate deformation of the droplet in Fig. 5(a), which is consistent with the analytical predictions. A nondimensional number $\lambda_{\tau_e} = \lambda_p/\lambda_c = \tau_{e,i}/\tau_{e,o}$ was introduced to predict the sense of flow direction within and outside the droplet and its effect on the droplet deformation. For $\lambda_{\tau_e} < 1$, the vortex direction within and outside the droplet is from the equator towards the pole of the droplet [60–63]. Here, the equator and the pole represent the endpoints of the droplet perpendicular and parallel to the applied electric field, respectively. Such counterclockwise flow in the first quadrant of the droplet agrees well with existing theoretical and experimental predictions [4].

In contrast, when $\lambda_c = 1.75$, we observe the oblate deformation of the droplet as shown in Fig. 5(b). Other nondimensional parameters are maintained the same as in the simulation performed in Fig. 5(a). Corresponding values of f_T and f_F are -5.65 and -4.6875 , respectively. Negative values of the discriminating functions suggest an oblate deformation of the droplet, which is consistent with the existing literature. For the simulation in Fig. 5(b), the value of $\lambda_{\tau_e} > 1$, which suggests that the flow direction within and outside the droplet is from the poles to the equator. As observed in Fig. 5(b), the sense of flow in the first quadrant of the droplet is clockwise. Such a prediction from the present model agrees with the existing analytical predictions [20,21].

The electrostatics of an initially spherical droplet can be analytically examined by neglecting the effect of surface charge convection. The free charges accumulate solely at the interface with zero net charge for a weakly conducting droplet

subjected to a uniform DC electric field. Such an unbounded buildup of charges with respect to time occurs in the Maxwell-Wagner polarization timescale [61,62,64] (τ_{MW}) as

$$q_s = 3\epsilon_i E_a \frac{1 - \lambda_{\tau_e}}{\lambda_c + 2} \left[1 - \exp\left(-\frac{t}{\tau_{MW}}\right) \right] \sin \theta. \quad (58)$$

Here, θ is the angle with the applied external electric field. The Maxwell-Wagner polarization timescale (τ_{MW}) is expressed as

$$\tau_{MW} = \frac{\epsilon_i + 2\epsilon_o}{\sigma_i + 2\sigma_o}, \quad (59)$$

where the subscripts i and o correspond to the droplet and the surrounding medium, respectively. Thus, from Eq. (58), we can deduce the polarity of accumulated charges at the interface from the response of the charge conduction of the two fluids. Such polarity is dependent on the ratio of λ_p and λ_c . When $\lambda_{\tau_e} < 1$, conduction within the droplet is faster than the surrounding medium. Hence, interfacial charge accumulation occurs mainly due to the mobile charges from the droplet. Consequently, the dipole of the droplet is oriented in the direction of the applied electric field. In Fig. 5(a), we observe that the positive charges accumulate in the upper hemisphere while the negative charges accumulate in the lower hemisphere. Such an accumulation of charges results in a dipole moment oriented in the direction of the applied electric field. Thus, the prediction of charge accumulation for $\lambda_{\tau_e} < 1$ from the present model agrees with existing analytical models.

In contrast to Fig. 5(a), we observe the orientation of the dipole moment is reversed in Fig. 5(b). As observed in Fig. 5(b), positive charges accumulate in the lower hemisphere of the droplet, while negative charges reside in the upper half of the droplet at the interface. Such an orientation of the charges results in a dipole moment acting opposite to the applied electric field. From Eq. (58), we can predict that, for $\lambda_{\tau_e} > 1$, charge conduction is faster in the suspending medium compared to the droplet. As such, free charges from the bulk of the suspending medium carried to the interface dominate over its counterparts from the droplet. As a result, the drop dipole orients in the direction opposite to the applied electric field.

Comparing Figs. 5(a) and 5(b), we further notice that the charge accumulation at the poles is higher in the case of oblate deformation compared to the prolate deformation. At steady state ($t \rightarrow \infty$), Eq. (58) can be expressed in terms of λ_c as

$$q_s = 3\epsilon_i E_a \frac{\lambda_c - \lambda_p}{\lambda_c^2 + 2\lambda_c} \sin \theta. \quad (60)$$

From Eq. (60), we observe that charge accumulation is inversely proportional to the electrical conductivity ratio λ_c . As such, the magnitude of charge accumulation is higher in oblate deformation than in prolate cases, even though all other parameters are the same.

Thus far, we qualitatively compared our results with existing analytical and experimental predictions. In Fig. 6, we quantify the predictions from the present model in terms of the deformation factor (D) and compare them with existing theoretical and numerical models. Figure 6 shows the deformation factor (D) as a function of increasing Ca_e .

Here, we consider two cases with $\lambda_p = 3.5$ and $\lambda_\mu = 1.4$ for varying Ca_e . In the prolate regime with positive deforma-

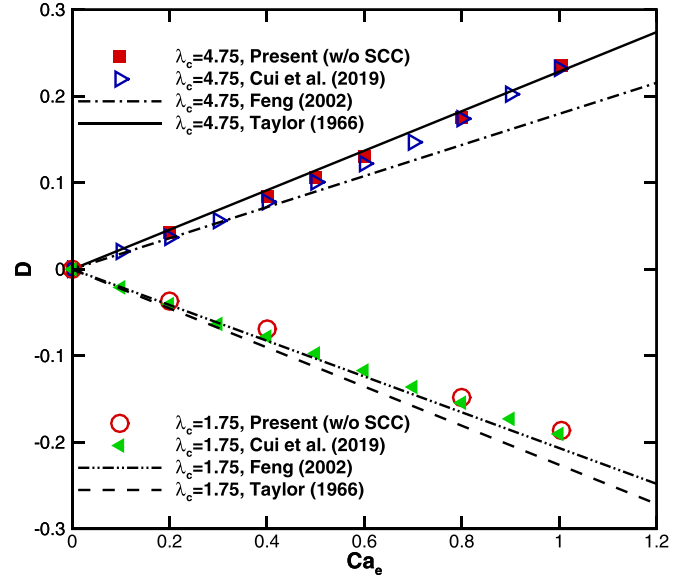


FIG. 6. Deformation of an LD droplet as a function of varying Ca_e without considering surface charge convection. Other dimensionless parameters are $\lambda_p = 3.5$ and $\lambda_\mu = 1.40$. For prolate deformations $\lambda_c = 4.75$ while, $\lambda_c = 1.75$ for negative deformations. Predictions from the present model are shown in red-filled squares and open circles for the prolate and oblate deformations, respectively. Taylor's analytical results are shown with solid and dashed lines for prolate and oblate deformations, respectively. Prolate and oblate deformations from Feng's analytical results are shown with dash-dotted and dash-dot-dotted lines, respectively. Predictions from decoupled numerical model are shown with a blue open right triangle and a solid green left triangle for prolate and oblate cases, respectively.

tions, we consider $\lambda_c = 4.75$. On the other hand, the value of λ_c is 1.75 for oblate or negative deformations. Equations (55) and (57) suggest that the amplitude of D monotonically increases with increasing Ca_e for both prolate ($f_T > 0$ or $f_F > 0$) and oblate ($f_T < 0$ or $f_F < 0$) deformations. Figure 6 shows a similar gradual increase in the magnitude of deformations for both prolate and oblate cases. We further observe that, in both the deformation regimes, our results without SCC agree well with the predictions from the existing LB-based numerical model, which were simulated by neglecting SCC [36]. In the case of prolate deformations, results from the present model marginally deviate from Taylor's analytical predictions for a range of Ca_e . In contrast, the results agree well with Feng's model for up to $Ca_e = 0.2$. Such deviation from Feng's first-order model is expected as the validity of the analytical solutions is limited to small values of Ca_e . The same scenario is observed in the case of oblate deformations. In oblate deformations, our predictions agree with Taylor's and Feng's theory for values of $Ca_e < 0.2$. However, we observe that, in this regime, the results from the present model are marginally underpredicted from theory for $Ca_e > 0.2$. Such behavior can be attributed to the diffuse nature of the interface.

C. Effect of SCC

Next, we study the effects of the SCC on droplet deformation. At stronger electric fields, convection at the interface

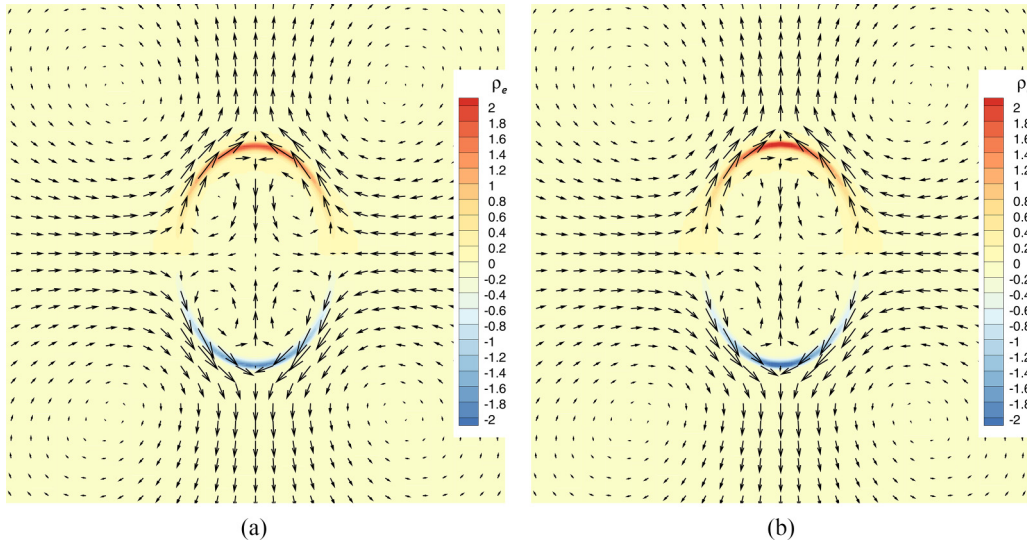


FIG. 7. Contour of charge accumulation and velocity vectors at $\lambda_\mu = 1.4$, $\lambda_c = 4.75$, $\lambda_p = 3.5$, and $Ca_e = 0.8$. (a) Prolate deformation without SCC. (b) Prolate deformation with SCC ($Re_e = 5.80$). The magnitude of charge accumulation at the poles is negligibly higher in the case with SCC than without SCC. No observable difference in the magnitude of deformation is noted between these two cases.

becomes dominant due to the larger finite values of Re_e , and the accumulated charges shift along the flow. Consequently, the electric stresses are affected at the interface and the deformation of the droplet deviates from the linear theory. In prolate deformations, such a nonlinear mechanism of SCC strengthens the deformation by accumulating similar additional charges at the poles. In contrast, deformation is weakened due to SCC when the drop shape is oblate spheroid as the charges are moved towards the equator from the poles. However, as previously reported [23,32], the effect of SCC on droplet deformation is different for prolate and oblate shapes, as we show them in Figs. 7 and 8. The parameters for these simulations are the same as in Table I. While the completely

coupled equations are solved by varying Re_e to study the effect of SCC, the charge advection term in Eq. (15) is neglected to simulate the cases without SCC.

As observed in Fig. 7, the effect of SCC is negligible in the prolate deformation regime. Such weak effects of SCC are not uncommon and have been reported in the existing literature for large deformation cases [32,61]. Figure 7(a) shows the electric charge and velocity vector contour without considering SCC. While in Fig. 7(b), we consider the effects of SCC and plot the same contours. The nondimensional parameters, λ_μ , λ_c , λ_p , and Ca_e for both these cases are 1.40, 4.75, 3.5, and 0.8, respectively. While no SCC for Fig. 7(a) was achieved by neglecting the convection term in Eq. (15), Re_e is finite for

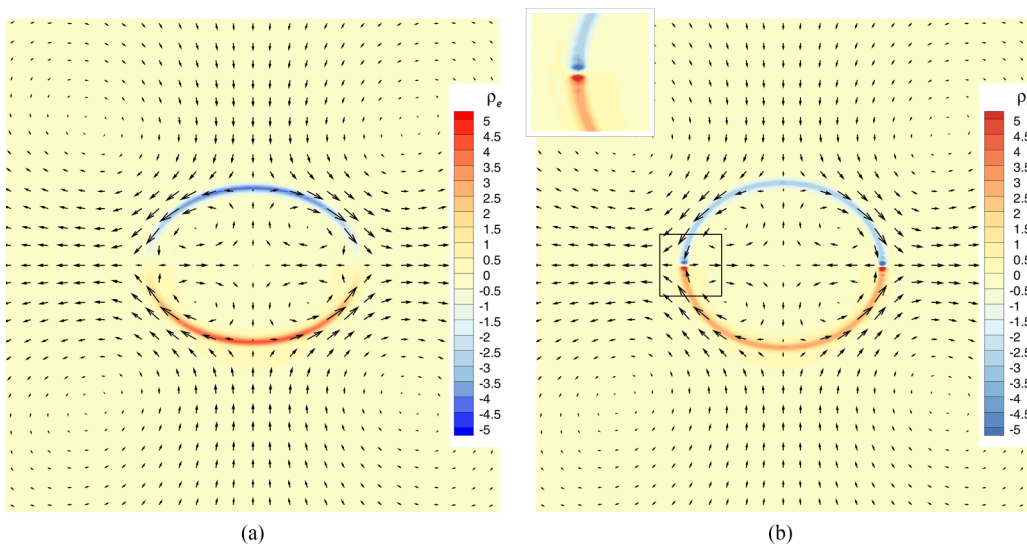


FIG. 8. Contour of charge accumulation and velocity vectors at $\lambda_\mu = 1.4$, $\lambda_c = 1.75$, $\lambda_p = 3.5$, and $Ca_e = 0.8$. (a) Oblate deformation without SCC ($Re_e = 0$). (b) Oblate deformation with SCC ($Re_e = 5.80$). While in the case without SCC, most of the charge accumulation occurs at the poles, the charges accumulate at the equator due to the SCC leading to a charge shock (inset). Moreover, the magnitude of charge accumulation is more than twice in the case with SCC compared to the one without SCC.

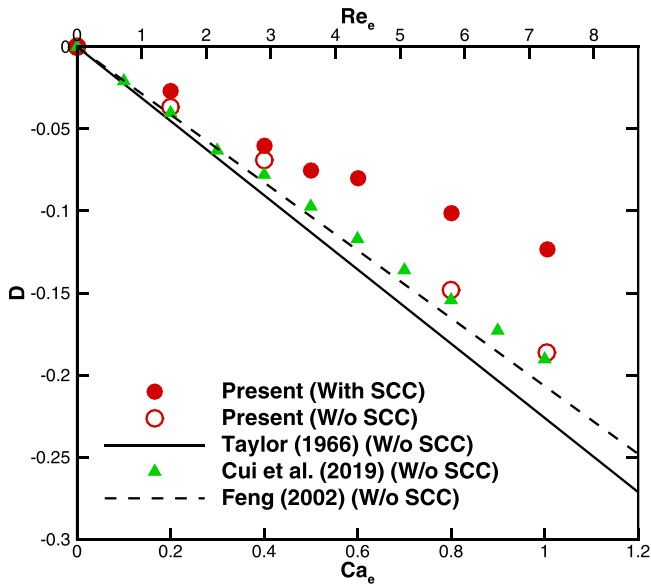


FIG. 9. Deformation as a function of Re_e and Ca_e at $\lambda_\mu = 1.4$, $\lambda_p = 3.5$, and $\lambda_c = 1.75$. Solid and dashed lines represent predictions from Taylor’s and Feng’s linearized analytical models, respectively. Solid and open red circles represent predictions from the present model for varying Re_e considering the effect of SCC and Ca_e neglecting SCC, respectively. Solid green triangles represent the decoupled solution for the deformation of an LD droplet without considering SCC by Cui *et al.* [36].

Fig. 7(b) with value 5.80. In such cases, SCC enhances the accumulation of charges at the poles when the deformation is a prolate spheroid with the equator-to-pole flow. Moreover, the drop is more conducting than the outer medium as $\lambda_{\tau_e} < 1$. Consequently, the interface behaves similarly to a highly conducting surface, thus reducing the tangential component of the electric stresses considerably [19]. As the Coulombic forces dominate the deformation in the LD regime, the effect of SCC is weakened due to the reduced presence of the tangential electric stresses. Moreover, increased accumulation of charges at the poles enhances the charge continuity leading to a weaker effect of SCC on prolate deformations [23]. Thus, we observe a negligible difference in the deformation between Figs. 7(a) and 7(b). Nonetheless, with stronger electric fields, the SCC will affect the prolate deformation of the droplets [18]. However, within the limit of Ca_e studied in this work, the effect of SCC is negligible in the prolate deformation regime.

In contrast to the previous case of prolate deformation in Fig. 7, we observe a strong effect of SCC in the case where the deformation of the droplet is an oblate spheroid with a pole-to-equator flow as shown in Fig. 8. For these contours, λ_μ , λ_c , λ_p , and Ca_e are 1.40, 1.75, 3.5, and 0.8, respectively. Figure 8(a) shows the flow circulations and electric charge contours for an initially spherical droplet neglecting the effect of SCC. Here we observe that the major charge accumulation occurs at the poles. Contrary to the case in Fig. 8(a), when the effect of SCC is taken into account with a finite value of $Re_e = 5.80$, the accumulated charges convect towards the equator from the pole in Fig. 8(b). At the steady state, we observe a maximum accumulation of countercharges from

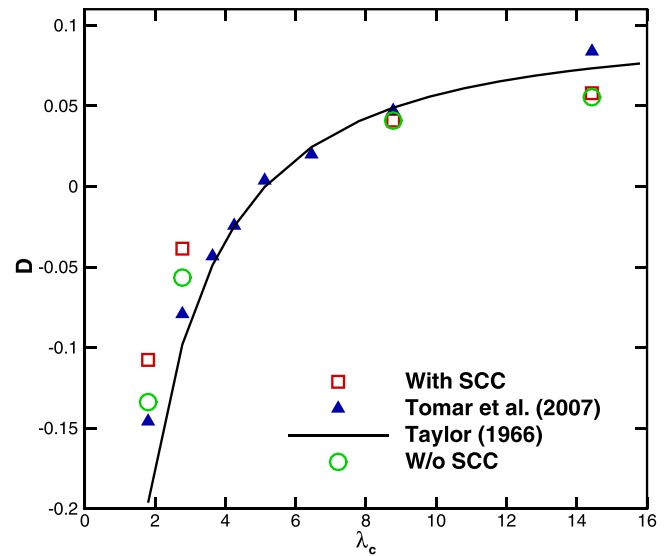


FIG. 10. Deformation as a function of the conductivity ratio of the disperse to the continuous phase. The solid black line represents the values predicted by Taylor’s analytical model. Solid blue triangles are the numerical predictions by Tomar *et al.* using coupled level-set and volume-of-fluid methods. Open red squares and green circles are predictions from the present model considering and neglecting the effects of SCC, respectively.

both hemispheres at the equator. Such an accumulation of opposite charges at the equator leads to a charge shock, as shown in the inset of Fig. 8(b). Such charge shock ultimately leads to an abrupt rise in charge accumulation [23,32] in the case of SCC-driven oblate deformations.

As discussed before, in the parametric limit considered herein, the effect of SCC is stronger in the oblate deformation regime compared to the prolate regime. Hence in the context of SCC, we limit our quantification and comparison of deformations to oblate flows in Fig. 9. Here, we show the deformation as a function of increasing electric Reynolds number. As observed in Fig. 9, deformation is less in SCC-driven flows compared to the cases where SCC is neglected. As mentioned, SCC reduces the accumulated charges at the poles in oblate deformations. The subsequent reduction of net electrostatic forces at the poles leads to a weaker deformation. Hence, we observe smaller deformation for SCC-driven flows in Fig. 9. For $Re_e < 2$, we note negligible deviation in the drop deformation from the analytical and decoupled numerical predictions, while at larger values of the Re_e effect of SCC is profound and should not be neglected. Moreover, such deviation from decoupled numerical predictions increases with increasing Re_e corresponding to the stronger electric fields. As the effect of SCC dominates over charge conduction at higher values of Re_e , it stabilizes the deformation of oblate droplets. Hence we observe an increasing deviation of deformation between numerical predictions with and without SCC.

We further quantify the effect of increasing electrical conductivity ratio on SCC in Fig. 10 and compare our numerical predictions with that of Tomar *et al.* [28] and Taylor’s analytical model. The physical parameters for the present study are summarized in Table II. The ratio of electrical permittivity

TABLE II. Notation and values of the physical properties of the fluids involved in comparison with Tomar *et al.* [28]. All other values are the same as used before.

Symbol	Description	Value
μ_i	Dynamic viscosity of dispersed phase	1×10^{-3} Pa s
ϵ_i	Absolute electrical permittivity of dispersed phase	3.94×10^{-10} C/V m
ϵ_o	Absolute electrical permittivity of continuous phase	3.94×10^{-11} C/V m

(λ_p) is 10. The ratio of electrical conductivities (λ_c) is varied from 1.80 to 14.4 by varying the conductivity of the droplet (σ_i). While the electric capillary number (Ca_e) for all the cases is 0.18, the electric Reynolds number (Re_e) is 1.25 for the cases with and without SCC. The magnitudes of other parameters remain unchanged as in Table I.

Figure 10 shows the droplet deformation as a function of increasing electrical conductivity ratio for cases considering and neglecting the effect of SCC. With increasing λ_c , the deformation transitions from oblate ($D < 0$) to prolate ($D > 0$) spheroidal shapes. Moreover, the solutions from the present numerical model of the decoupled problem by neglecting SCC marginally agree with analytical solutions for weak deformations. In addition, we observe that the deformations in our simulations are consistent with the results obtained by Tomar *et al.* [28].

Similar to Fig. 7, we observe a weak effect of SCC on prolate deformations when $\lambda_c > 6$. Deformations predicted within this regime with and without the effect of SCC coincide. Such a prediction of the weak effect of SCC in the prolate regime at larger values of λ_c agrees well with the existing literature [31]. On the other hand, with decreasing λ_c , the droplet transitions towards oblate deformations regime below $\lambda_c \approx 6$. In this regime, the difference in the predicted deformations between with and without SCC cases increases with decreasing λ_c . Such a prediction agrees with the existing theory [31] due to the charge shock resulting from the SCC.

In the previous simulations, we limited the deformation considering the effect of SCC to small values ($D \sim 0.1$). Here, we present charge contours corresponding to a case with large deformations ($D > 0.10$). Table III gives the parameters used in these simulations. All other parameters are reused from the comparison with Tomar *et al.* [28]. Figure 11 shows the temporal evolution of charge accumulation for a large deformation case with $\lambda_\mu = 1$, $\lambda_c = 0.1$, $\lambda_p = 2.0$, $Ca_e = 0.4$, and $Re_e = 22.2$. Initially, the charges accumulate at the poles as observed in Fig. 11(a). When the SCC gradually overcomes the charge accumulation, we observe an equatorial charge accumulation leading to a charge shock [see

Fig. 11(b)]. The deformation index obtained in this case is -0.30 , suggesting a large deformation as defined by Alidoost and Reza Pissevar [32].

However, the deformation is yet to become steady at this stage. As time progresses, we observe another transition from such equatorial charge shock to thin sheet formation around the droplet [Fig. 11(c)]. Finally, in Fig. 11(d), we observe equatorial streaming where the thin sheet breaks up from the parent droplet. The deformation index before the breakup is estimated to be -0.581 . As such, unlike Alidoost and Reza Pissevar [32], we observe a different breakup mode. Such behavior can be attributed to the difference in the magnitude of electrical conductivity of the fluids used in the present case and in Alidoost and Reza Pissevar [32]. Nonetheless, these results are in agreement with the existing literature [63].

V. CONCLUSION

In the present work, we developed a coupled LB and FD method-based numerical framework to study the transient EHD flows by solving the completely coupled Taylor-Melcher LD model. Unlike previous LB-based models, the present methodology includes nonlinear surface-charge convection with directional derivatives at the interface. Considering such directional derivatives helps to eliminate the miscalculation of the interfacial discontinuities arising while using the volumetric derivatives at the interface.

First, we qualitatively validate the present model by comparing the charge accumulation, dipole orientation, and the vortices generated inside and outside the droplet with the existing literature [20,36]. All such predictions from the present model agree well with the existing theoretical predictions for both oblate and prolate regimes with acceptable accuracy. The quantitative comparisons of the predicted deformations from the present model without SCC show good agreement with the analytical expressions by Taylor [20] and Feng [59], and other LB-based numerical predictions [36].

We further demonstrate the capability of the present model for SCC-dominated flows. We compared the charge accumulation for the cases with and without SCC and with the

TABLE III. Notation and values of the physical properties of the fluids involved in simulations with large deformation with SCC. All other values are the same as used in Table II.

Symbol	Description	Value
ϵ_i	Absolute electrical permittivity of dispersed phase	8×10^{-10} C/V m
ϵ_o	Absolute electrical permittivity of continuous phase	4×10^{-11} C/V m
σ_i	Electrical conductivity of dispersed phase	1.275×10^{-8} S/m
ϵ_o	Electrical conductivity of continuous phase	1.275×10^{-7} S/m

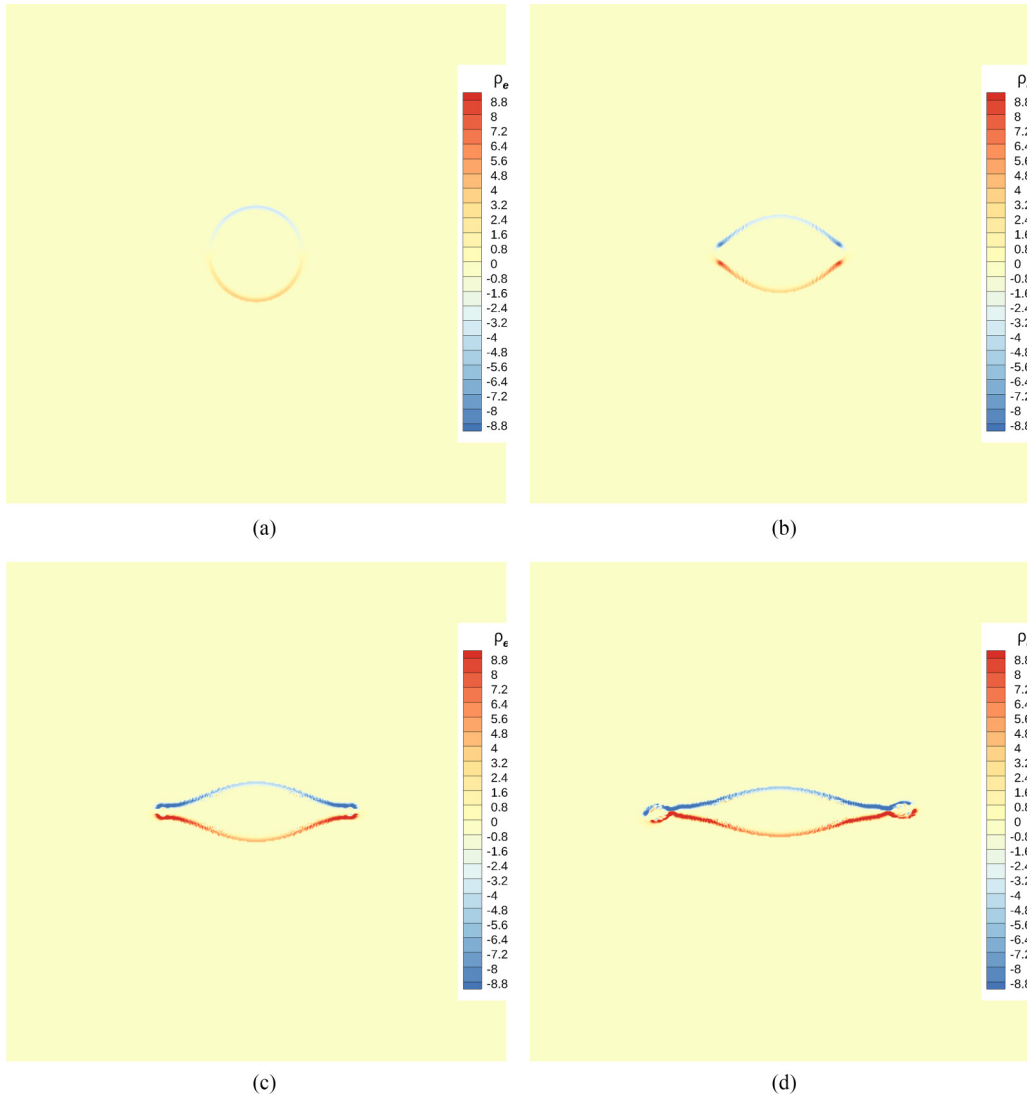


FIG. 11. Contour of charge accumulation for large oblate deformation with SCC with $\lambda_\mu = 1$, $\lambda_c = 0.1$, $\lambda_p = 2.0$, $Ca_e = 0.4$, and $Re_e = 22.2$ at different nondimensional time steps: (a) 10.6, (b) 31.8, (c) 63.7, (d) 88.5.

findings in the existing literature. The qualitative comparison of charge accumulation and deformation within the prolate and oblate deformation regime with SCC agreed well with the existing literature. In addition, we were able to observe the presence of charge shock at the equator for oblate deformations, which has not been observed in other LB-based numerical models. The present model further predicts the slightly increased charge accumulation due to SCC at the poles for the prolate deformations suggesting a weaker effect of SCC on prolate deformations. In contrast, the predicted charge shock in oblate deformation induced a strong nonlinear effect on the drop deformations. Such predictions prove the potential of the present simulation approach to make qualitative predictions of SCC-dominated flows. The predicted nonlinear trend in drop deformations in the oblate regime quantitatively validates the present model for EHD flows with SCC. Additionally, such quantification explains the reason for stronger nonlinearity in the oblate deformation regime compared to prolate deformations. Corresponding to moderate Ca_e , the effect of the conductivity ratio on SCC and

subsequent deformation was also compared with Tomar *et al.* [28]. The quantitative comparison of deformation between with and without SCC at moderate Ca_e successfully showed the decrease and increase in deformation due to SCC in the oblate and prolate regimes, respectively. Thus, unlike other existing LB-based models, we are able to explain the reason behind the weak effect of SCC in prolate deformation and a strong effect on the oblate deformation of a droplet.

All these predictions indicate the capability of the present numerical model to successfully simulate the SCC-dominated EHD flows. Such flows include but are not limited to, the electrorotation of an LD droplet at stronger electric fields and EHD droplet generation in complex geometries like T-shaped [12,65] and cross-flow microchannels.

ACKNOWLEDGMENTS

The authors acknowledge funding received from the Ministry of Education, Government of India, under Grant No. IMP/2018/000422. S.S.B. acknowledges financial

support from SERB under MATRICS scheme (Grant No. MTR/022/000080). H.S.B. is grateful to Dr. Yogesh G.

Bhumkar for his insightful comments on the finite difference method.

-
- [1] J. R. Melcher and G. I. Taylor, *Annu. Rev. Fluid Mech.* **1**, 111 (1969).
- [2] G. C. Simpson and G. T. Walker, *Phil. Trans. R. Soc. Lond. A* **209**, 379 (1909).
- [3] D. C. Blanchard, *Prog. Oceanogr.* **1**, 73 (1963).
- [4] G. I. Taylor, *Proc. R. Soc. London A* **280**, 383 (1964).
- [5] G. I. Taylor and M. D. Van Dyke, *Proc. R. Soc. London A* **313**, 453 (1969).
- [6] O. Yogi, T. Kawakami, M. Yamauchi, J. Y. Ye, and M. Ishikawa, *Anal. Chem.* **73**, 1896 (2001).
- [7] J.-U. Park, M. Hardy, S. J. Kang, K. Barton, K. Adair, D. K. Mukhopadhyay, C. Y. Lee, M. S. Strano, A. G. Alleyne, and J. G. Georgiadis, *Nat. Mater.* **6**, 782 (2007).
- [8] A. K. Singh, R. K. Srivastava, and S. S. Bahga, *Phys. Rev. Fluids* **7**, 063701 (2022).
- [9] I. Hayati, A. I. Bailey, and T. F. Tadros, *J. Colloid Interface Sci.* **117**, 205 (1987).
- [10] M. Cloupeau and B. Prunet-Foch, *J. Aerosol Sci.* **25**, 1021 (1994).
- [11] A. M. Gañán Calvo, *J. Fluid Mech.* **507**, 203 (2004).
- [12] M. Shojaeian and S. Hardt, *Appl. Phys. Lett.* **112**, 194102 (2018).
- [13] B. Aramide, A. Kothandaraman, M. Edirisinghe, S. N. Jayasinghe, and Y. Ventikos, *Langmuir* **35**, 10203 (2019).
- [14] R. Singh, S. S. Bahga, and A. Gupta, *J. Fluid Mech.* **905**, A29 (2020).
- [15] A. D. Griffiths and D. S. Tawfik, *Trends Biotechnol.* **24**, 395 (2006).
- [16] J. R. Melcher and C. V. Smith, *Phys. Fluids* **12**, 778 (1969).
- [17] D. A. Saville, *Annu. Rev. Fluid Mech.* **29**, 27 (1997).
- [18] R. Sengupta, L. M. Walker, and A. S. Khair, *J. Fluid Mech.* **833**, 29 (2017).
- [19] O. Vizika and D. A. Saville, *J. Fluid Mech.* **239**, 1 (1992).
- [20] G. I. Taylor, A. D. McEwan, and L. N. J. de Jong, *Proc. R. Soc. London A* **291**, 159 (1966).
- [21] S. Torza, R. G. Cox, S. G. Mason, and G. I. Taylor, *Phil. Trans. R. Soc. Lond. A* **269**, 295 (1971).
- [22] O. O. Ajayi and T. G. Cowling, *Proc. R. Soc. London A* **364**, 499 (1978).
- [23] D. Das and D. Saintillan, *J. Fluid Mech.* **810**, 225 (2017).
- [24] E. Lac and G. M. Homsy, *J. Fluid Mech.* **590**, 239 (2007).
- [25] T. Tsukada, T. Katayama, Y. Ito, and M. Hozawa, *J. Chem. Eng. Jpn.* **26**, 698 (1993).
- [26] J. Q. Feng and T. C. Scott, *J. Fluid Mech.* **311**, 289 (1996).
- [27] G. Supeene, C. R. Koch, and S. Bhattacharjee, *J. Colloid Interface Sci.* **318**, 463 (2008).
- [28] G. Tomar, D. Gerlach, G. Biswas, N. Alleborn, A. Sharma, F. Durst, S. Welch, and A. Delgado, *J. Comput. Phys.* **227**, 1267 (2007).
- [29] J. M. López-Herrera, S. Popinet, and M. A. Herrada, *J. Comput. Phys.* **230**, 1939 (2011).
- [30] J. A. Lanauze, L. M. Walker, and A. S. Khair, *J. Fluid Mech.* **774**, 245 (2015).
- [31] D. Das and D. Saintillan, *J. Fluid Mech.* **829**, 127 (2017).
- [32] M. Alidoost and A. Reza Pishevar, *J. Fluids Eng.* **140**, 121201 (2018).
- [33] A. L. Kupershtokh and D. A. Medvedev, *J. Electrostat.* **64**, 581 (2006).
- [34] M. Lauricella, S. Melchionna, A. Montessori, D. Pisignano, G. Pontrelli, and S. Succi, *Phys. Rev. E* **97**, 033308 (2018).
- [35] R. Singh, S. S. Bahga, and A. Gupta, *Eur. J. Mech. B Fluids* **74**, 167 (2019).
- [36] Y. Cui, N. Wang, and H. Liu, *Phys. Fluids* **31**, 022105 (2019).
- [37] X. Liu, Z. Chai, and B. Shi, *Commun. Comput. Phys.* **30**, 1346 (2021).
- [38] Y. Zhang, Z. Su, K. Luo, and H. Yi, *Phys. Fluids* **34**, 043601 (2022).
- [39] X. Liu, Z. Chai, and B. Shi, *Phys. Fluids* **31**, 092103 (2019).
- [40] K. Luo, J. Wu, H.-L. Yi, and H.-P. Tan, *Phys. Fluids* **32**, 123606 (2020).
- [41] D. d’Humières, Generalized lattice-Boltzmann equations, in *Rarefied Gas Dynamics: Theory and Simulations*, edited by D. P. Weaver and B. D. Shizgal, Progress in Astronautics and Aeronautics, Vol. 159 (American Institute of Aeronautics and Astronautics, Washington, D.C, 1992), pp. 450–458.
- [42] I. Halliday, R. Law, C. M. Care, and A. Hollis, *Phys. Rev. E* **73**, 056708 (2006).
- [43] W. F. Hasan, H. Farhat, S. Kondaraju, and T. Singh, *Computers & Fluids* **165**, 188 (2018).
- [44] S. Popinet, *Annu. Rev. Fluid Mech.* **50**, 49 (2018).
- [45] H. S. Basu, S. S. Bahga, and S. Kondaraju, *Proc. R. Soc. A* **476**, 20200423 (2020).
- [46] T. Krüger, H. Kusumaatmaja, A. Kuzmin, O. Shardt, G. Silva, and E. M. Viggen, *The Lattice Boltzmann Method: Principles and Practice*, 1st ed., Graduate Texts in Physics (Springer International Publishing, New York, 2017).
- [47] A. K. Gunstensen, D. H. Rothman, S. Zaleski, and G. Zanetti, *Phys. Rev. A* **43**, 4320 (1991).
- [48] P. Lallemand and L.-S. Luo, *Phys. Rev. E* **61**, 6546 (2000).
- [49] D. d’Humières, I. Ginzburg, M. Krafczyk, P. Lallemand, and L.-S. Luo, *Phil. Trans. R. Soc. Lond. A* **360**, 437 (2002).
- [50] Z. Chai and B. Shi, *Phys. Rev. E* **102**, 023306 (2020).
- [51] L. Scarbolo, D. Molin, P. Perlekar, M. Sbragaglia, A. Soldati, and F. Toschi, *J. Comput. Phys.* **234**, 263 (2013).
- [52] M. C. Sukop and D. T. Thorne, Jr., *Lattice Boltzmann Modeling: An Introduction for Geoscientists and Engineers* (Springer, Berlin, 2006).
- [53] A. L. Kupershtokh, D. A. Medvedev, and D. I. Karpov, *Comput. Math. Appl.* **58**, 965 (2009).
- [54] J. Brackbill, D. Kothe, and C. Zemach, *J. Comput. Phys.* **100**, 335 (1992).
- [55] M. Latva-Kokko and D. H. Rothman, *Phys. Rev. E* **71**, 056702 (2005).
- [56] I. Halliday, A. P. Hollis, and C. M. Care, *Phys. Rev. E* **76**, 026708 (2007).
- [57] D. Anderson, J. C. Tannehill, R. H. Pletcher, R. Munipalli, and V. Shankar, *Computational Fluid Mechanics and Heat Transfer*,

- 3rd ed., Computational and Physical Processes in Mechanics and Thermal Sciences (CRC Press, Boca Raton, FL, 2020).
- [58] A. H. Van Tuyl, *Mathematics of Computation* **63**, 229 (1994).
- [59] J. Q. Feng, *J. Colloid Interface Sci.* **246**, 112 (2002).
- [60] T. B. Jones, *Electromechanics of Particles* (Cambridge University Press, Cambridge, England, 2005).
- [61] J. A. Lanauze, L. M. Walker, and A. S. Khair, *Phys. Fluids* **25**, 112101 (2013).
- [62] M. Ouriemi and P. M. Vlahovska, *Langmuir* **31**, 6298 (2015).
- [63] P. M. Vlahovska, *Annu. Rev. Fluid Mech.* **51**, 305 (2019).
- [64] P. F. Salipante and P. M. Vlahovska, *Phys. Fluids* **22**, 112110 (2010).
- [65] S. K. Jena, S. S. Bahga, and S. Kondaraju, *Phys. Fluids* **33**, 032120 (2021).